Ore Geology Reviews 139 (2021) 104453

Contents lists available at ScienceDirect

Ore Geology Reviews

journal homepage: www.elsevier.com/locate/oregeorev

Nanoinclusions in zoned magnetite from the Sossego IOCG deposit, Carajás, Brazil: Implication for mineral zoning and magnetite origin discrimination

Xiao-Wen Huang [a,b,c,*], Georges Beaudoin [b,c]

[a] State Key Laboratory of Ore Deposit Geochemistry, Institute of Geochemistry, Chinese Academy of Sciences, Guiyang 550081, China
[b] Département de géologie et de génie géologique, Université Laval, Québec, QC G1V 0A6, Canada
[c] Research Center on the Geology and Engineering of Mineral Resources (E4m), Université Laval, Québec, QC G1V 0A6, Canada

ARTICLE INFO

Keywords:
Oscillatory zoning
Magnetite
Nanoinclusions
Transmission electron microscopy
Sossego
IOCG

ABSTRACT

Compositional zoning is common in magnetite from different geological environments, but its formation mechanism remains controversial. Here, we characterize micron- to nano-scale textural and chemical variations in zoned magnetite from the Sossego iron oxide-copper–gold deposit (Carajás, Brazil) using electron probe microanalyzer (EPMA) and transmission electron microscopy (TEM). Lack of porosity and of a reaction front at both the micron and nanometer scales indicates that compositional zoning in magnetite is a pristine texture formed during crystal growth, rather than a secondary texture due to dissolution and reprecipitation reaction. TEM energy dispersive X-ray spectrometry analyses and mapping identify four types of nanoinclusions in zoned magnetite: 1) Mg-Fe-Al silicates, most likely amphibole, 2) Fe-Ti oxides, mainly ilmenite, 3) pyroxene, 4) Si-rich magnetite. The formation of ilmenite nanoinclusions in Sossego magnetite is possibly due to oxy-exsolution of ulvöspinel from Ti-rich magnetite, whereas nanoinclusions of other minerals likely formed by local supersaturation in the fluid boundary layer, followed by magnetite crystal entrapment. Compositional zoning in magnetite likely formed by a self-organization process where fluid composition fluctuations are feedback responses for an evolving fluid system far from equilibrium, rather than cyclic variations in external factors such as temperature and oxygen fugacity. Saturation of silicate minerals results in relative depletion of Si, Ca, and Al in boundary layer fluids, and formation of inclusion-poor zone depleted in these elements. Nanoinclusions in magnetite highlight the importance of textural characterization when using in situ chemical composition to discriminate the origin of magnetite. In addition, the assemblages of nanoinclusions in magnetite can be used to complement the discrimination of magnetite origins.

1. Introduction

The chemical composition of magnetite from a range of rocks and mineral deposits has been widely used to reveal petrogenesis and ore genesis (e.g., Dupuis and Beaudoin, 2011; Dare et al., 2012; Nadoll et al., 2012; Huang et al., 2013, 2019a, Huang et al., 2019b; Knipping et al., 2015; Canil et al., 2016; Canil and Lacourse, 2020), and used as a tool in mineral exploration (e.g., Dupuis and Beaudoin, 2011; Makvandi et al., 2016; Pisiak et al., 2017). However, with increased studies, the empirical diagrams based on trace element contents or ratios of magnetite are considered to have some limitations due to extremely various magnetite chemistry at different scales (Gourcerol et al., 2016; Velasco et al., 2016; Broughm et al., 2017; Wen et al., 2017; Huang et al., 2019b). The various composition of magnetite at the scale of a deposit type, a deposit, or a paragenetic stage, have been ascribed to variations in external factors such as temperature, oxygen fugacity, sulfur fugacity and melt/fluid composition (Dare et al., 2012; Acosta-Gongora et al., 2014; Nadoll et al., 2014; Huang et al., 2015a, b, 2016; Knipping et al., 2015; Liu et al., 2015; Canil et al., 2016; Sun et al., 2017; Li et al., 2018). A magnetite grain of several to hundreds of microns can also show compositional heterogeneity, which has been explained by micro inclusions or chemical zoning in magnetite (Dupuis and Beaudoin, 2011; Huberty et al., 2012; Huang et al., 2014; Xu et al., 2014; Cook et al., 2016; Deditius et al., 2018; Ciobanu et al., 2019; Verdugo-Ihl et al., 2020). However, the mineralogy and distribution of inclusions in magnetite are not well studied, in particular, when these inclusions have nanometer sizes. Zoned magnetite, composed of zones rich or poor in one or several elements, has been found in different types of deposits

* Corresponding author at: State Key Laboratory of Ore Deposit Geochemistry, Institute of Geochemistry, Chinese Academy of Sciences, Guiyang 550081, China.
E-mail address: huangxiaowen@mail.gyig.ac.cn (X.-W. Huang).

https://doi.org/10.1016/j.oregeorev.2021.104453
Received 17 April 2021; Received in revised form 26 August 2021; Accepted 30 August 2021
Available online 2 September 2021

(Westendorp et al., 1991; Dare et al., 2015; Knipping et al., 2015; Deditius et al., 2018; Ciobanu et al., 2019; Huang and Beaudoin, 2019), and is thus an excellent example for studying element or mineral behavior during crystal growth. Moreover, the detailed textural and compositional studies of zoned magnetite will provide important constraints on their formation mechanism.

In this study, we present electron probe microanalyzer (EPMA) and high-resolution transmission electron microscopy (TEM) analyses of well-studied zoned magnetite from the Sossego iron oxide-copper–gold (IOCG) deposit, Carajás, Brazil. The aim of this study is to: 1) characterize the textural and compositional variation of zoned magnetite; 2) investigate the sitting of trace elements in magnetite; 3) identify the mineralogy and distribution of inclusions (μm to nm scale) in magnetite; and (4) constrain the formation mechanism of inclusion-rich, zoned magnetite. This study highlights that nanometer-scale mineral inclusions are common in zoned magnetite from magmatic-hydrothermal deposits such as IOCG (Ciobanu et al., 2019), IOA (Deditius et al., 2018), and Fe skarns (Yin et al., 2019) and that it is critical to consider these nanometer inclusions to interpret in-situ major and trace element data. The mineral assemblages at the nano-scale have essential implications for the discrimination between igneous and hydrothermal magnetite.

2. Geology of the Sossego deposit and sample information

Sample in this study was collected from the Sossego Cu-Au deposit in the Carajás Mineral Province of Brazil, one of the world's largest IOCG metallogenic provinces on Earth (Xavier et al., 2012) (Fig. 1a). The Sossego deposit is hosted by granitic and gabbroic intrusions, and felsic metavolcanic rocks (Monteiro et al., 2008a) (Fig. 1b). The deposit consists of two groups of orebodies, Sequeirinho–Pista–Baiano (SPB) and Sossego–Curral (SC) (Fig. 1b), which have different alteration types and formation ages. The Neoarchean (ca. 2.7 Ga) SPB orebodies are composed of deeper-level magnetite ± apatite and albite-actinolite-rich zones formed under relatively high-temperature (>500 °C) conditions, whereas the Paleoproterozoic (ca. 1.90–1.88 Ga), shallow-level, SC orebodies are characterized by lower-temperature (<300 °C) sericite, chlorite, epidote, hematite, and carbonate alteration (Monteiro et al., 2008a; Moreto et al., 2015). Fluids responsible for early calcic–sodic

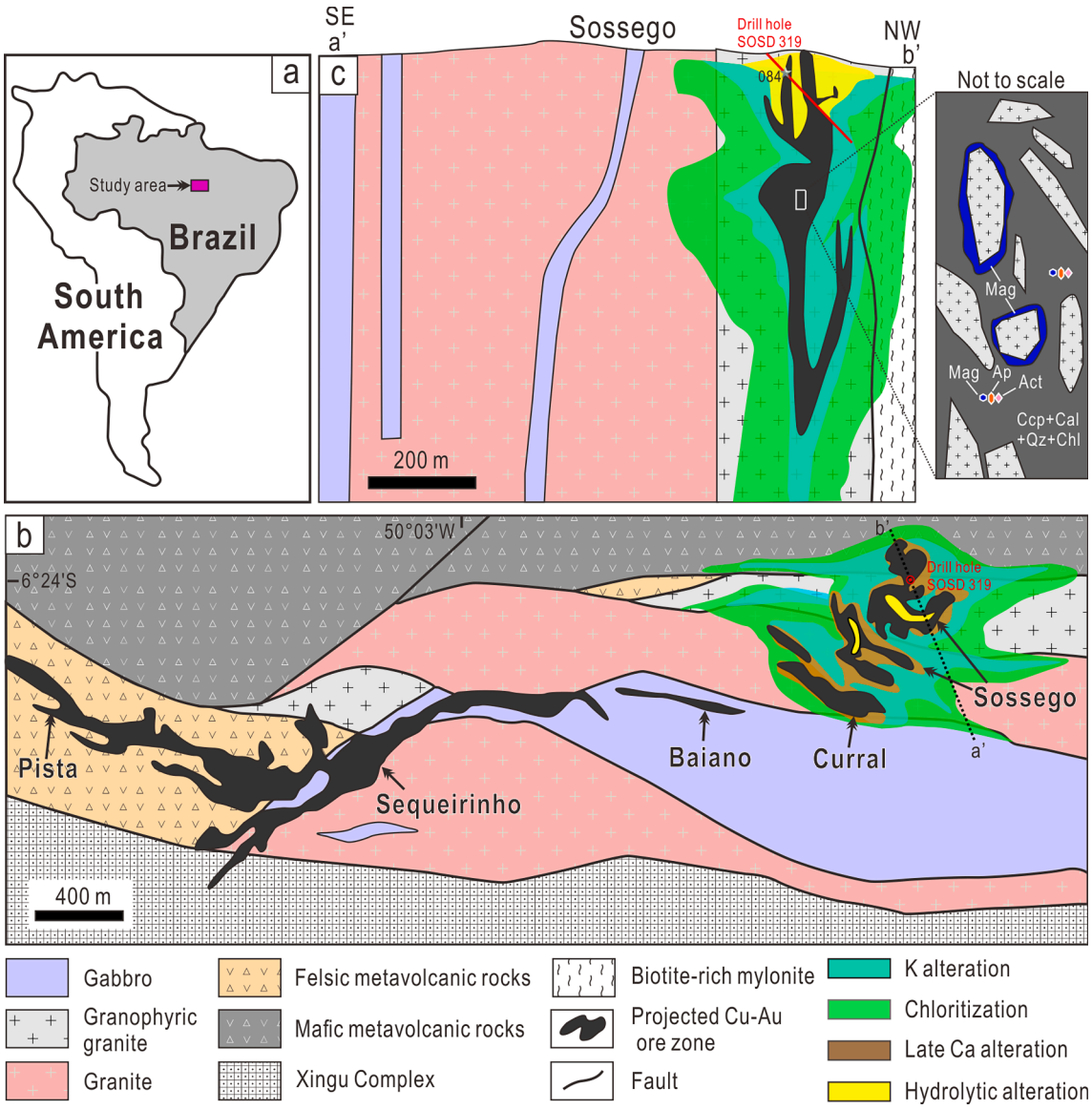

Fig. 1. (a) The location of study area in Brazil. (b) Simplified geological map of the Sossego IOCG deposit showing the distribution of different orebodies. (c) Simplified cross-section of the Sossego orebody indicating the sample location. Hydrothermal alteration zones around Sossego-Curral orebodies are marked in (b) and (c). A cartoon in (c) is used to characterize brecciated ores at Sossego orebody (Modified from Monteiro et al., 2008a, b). Abbreviations: Act-actinolite; Ap-apatite; Cal-calcite; Ccp-chalcopyrite; Chl-chlorite; Mag-magnetite; Qz-quartz.

alteration are mainly formation/metamorphic or magmatic in origin, whereas those formed the late low-temperature K-Fe alteration are dominated by meteoric water (Monteiro et al., 2008a). The estimated temperature for the calcic-sodic alteration is 500 ± 25 °C based on oxygen isotope composition of albite-actinolite pair, whereas actinolite-magnetite pair gives a temperature of 550 ± 25 °C for calcic-iron alteration (Monteiro et al., 2008a). It has been proposed that the mixing of high-temperature (>500 °C) hydrothermal fluids with meteoric water resulted in the precipitation of chloride-complexed metals (Monteiro et al., 2008b).

The Sossego orebody is mainly hosted by granophyric granite, and minor mineralization also occur in granite and felsic metavolcanic rocks (Fig. 1b, c). Early sodic–calcic alteration and massive magnetite bodies are poorly developed in the Sossego ore zone (Monteiro et al., 2008b). Locally albite-rich veinlets are observed within the host rocks. Widespread potassic alteration is represented by the mineral assemblages of biotite + magnetite + quartz and potassium feldspar + calcite + barite + uraninite + sphalerite + galena (Monteiro et al., 2008b) (Fig. 1b, c). The potassic alteration is closely related to Cu-Au mineralization, which is followed by fracture-controlled chlorite and hydrolytic (sericite-hematite-quartz) alteration (Xavier et al., 2012) (Fig. 1b, c). The Sossego orebody is strongly brecciated. The breccias are composed of angular to rounded fragments of potassic-altered granitic rocks rimmed by magnetite, whereas the matrix consists of hydrothermal minerals such as chalcopyrite, quartz, calcite, and chlorite with different proportions (Monteiro et al., 2008b) (Fig. 1c). Chalcopyrite-rich matrix characterizes some ore breccias in the center of ore body. Veins and breccias are filled by a mineral assemblage of magnetite, actinolite, apatite, biotite, calcite, epidote and minor pyrite and chalcopyrite (Monteiro et al., 2008a).

Sample 084 was collected at a depth of 74.1 m from the core of drillhole SOSD 319, which cuts the Sossego orebody (Fig. 1c). This sample is selected for this study because zoned magnetite grains are common in this sample and most of them are also Ti-rich (up to 1.8 wt% Ti) (Huang and Beaudoin, 2019). Monteiro et al. (2008b) also noted that magnetite from the Sossego orebody was richer in Ti than those from SPB orebodies. Sample 084 is from an ore breccia composed of ~ 90 modal% sulfides (mainly chalcopyrite), ~5 modal% magnetite and ~ 5 modal% other minerals (Fig. 2a). Sample 084 has a mineral assemblage of magnetite, actinolite, and apatite that is cemented by chalcopyrite (Fig. 2a). The magnetite-apatite-actinolite assemblage represents local high-temperature Ca-Fe alteration at Sossego (Huang et al., 2019a), similar to more widespread (Na)-Ca-Fe alteration assemblage of SPB orebodies (Monteiro et al., 2008a). In different areas of the thin section, the mineral proportion is subtly different and other minerals such as quartz, chlorite, and monazite are locally present (Fig. 2b-f). Magnetite is mainly subhedral to anhedral, with the grain size of < 100 μm to > 1 mm. Magnetite is in equilibrium with actinolite and apatite, and was replaced by chalcopyrite (Fig. 2b, c, f). Actinolite grows within magnetite grains (Fig. 2b, c) or along the margin of magnetite grains (Fig. 2d, e). Apatite can be coarse-grained euhedral crystals (up to 1 mm) associated with magnetite (Fig. 2f), or occurs as small inclusions in magnetite (Fig. 2c). Apatite is sometimes crosscut and replaced by quartz and chalcopyrite (Fig. 2f). Monazite is widespread within coarse-grained apatite (Fig. 2f).

3. Analytical methods

3.1. EPMA analyses

The thin section containing magnetite was examined using optical microscopy and back-scattered electron (BSE) imaging to determine mineral assemblages and microtextures of magnetite grains. High-contrast BSE images and compositional analyses of magnetite were carried out at Université Laval using a CAMECA SX-100 EPMA, equipped with five wavelength-dispersive spectrometers. Analyses were performed using a 5-μm diameter beam, a 15 kV voltage, a current of 20 nA for Fe and 100 nA for minor and trace elements. Analytical conditions are similar to those described by Huang and Beaudoin (2019). The concentrations of elements were calculated based on a series of natural and synthetic standards, simple oxides (GEO Standard Block of P and H Developments) and natural minerals (Mineral Standard Mount MINM 25–53, Astimex Scientific) (Jarosewich et al., 1980). Each analysis includes 15–20 s background signal and 20–40 s X-ray peak collection for different elements. Average detection limits are 433 ppm for Fe, 101 ppm for Zn, 84 ppm for Cu, 60 ppm for Ni, 40–60 ppm for V, Cr, Mn, and 14–32 ppm for K, Ca, Ti, Al, Si, Mg, and P. Wavelength dispersive spectrometer (WDS) X-ray maps were collected using a 1 μm beam, 15 kV accelerating voltage, 100 nA beam current, and a counting time of 20 ms for each pixel to yield a resolution of 512 × 512 pixels.

3.2. TEM analyses

TEM thin foils were prepared within a Helios G4 PFIB UXe DualBeam Xeon Plasma Focused Ion Beam (FIB), located at the Canadian Center for Electron Microscopy (CCEM), McMaster University. By going through in-situ lift-out steps, foils of approximately 20 × 15 × 1 μm^3 representing cross-sections perpendicular to, and across the magnetite zones, were cut directly from the Mag-1 grain in the polished thin section, using 30 kV Xe ion beams. The foils were protected initially by electron-deposited Pt + C followed by Xe deposition. Thin foils were glued to Cu grids. After that, electron transparent specimens were obtained with progressively reduced currents from 1.0 to 0.3 nA at 30 kV and polished with stepped low kV beams until 2 kV.

Transmission electron microscopy was carried out at CCEM using a FEI Titan 80–300 TEM equipped with CEOS (Corrected Electron Optical Systems GmbH) image corrector resulting in a point resolution of 0.8 Å. The TEM is equipped with a Tridiem imaging filter (Gatan), a high-angle annular dark field detector (HAADF, Fishione), and an energy dispersive X-ray spectrometer (EDS) (Oxford Instruments) with an ultrathin window. X-ray data were collected at an acceleration voltage of 200 kV, using an acquisition time of 120 s and 2 h for point analysis and elemental maps, respectively. Diffraction patterns of minerals are acquired from high-resolution TEM images by fast Fourier transform using the software DigitalMicrograph.

4. Results

4.1. Magnetite petrography and geochemistry

Magnetite grains in the sample 084 are dominated by subhedral crystals with grain size up to 1 mm. The mineral inclusions in magnetite are mainly actinolite, apatite, and chalcopyrite with minor chlorite (Figs. 2c, e, 3a). Magnetite is commonly replaced by chalcopyrite, indicating that magnetite formed before the main Cu mineralization (Fig. 2e). The studied magnetite grain shows oscillatory zoning under high-resolution BSE imaging, and the FIB foil crosscuts the contact between dark gray and light gray zones (Fig. 3a). The dark gray zone comprises large amounts of mineral inclusions smaller than 1 μm, whereas both dark gray and light gray zones contain needle-like mineral inclusions that are 1 to 5 μm long (Fig. 3a). Dark gray zones contain a high proportion of inclusions, whereas light gray zones have a low abundance of inclusions. EPMA mapping of a selected area in the magnetite grain shows Al, Si, Mg, and Ca-bearing zones that correspond to the growth zoning (Fig. 3b). Mineral inclusions, such as Fe-Ti oxides and Al-bearing spinel, are identified by the heterogeneous distribution of Ti and Al (Fig. 3b). Manganese is homogeneously distributed in magnetite except for Mn-rich inclusions along a fracture in magnetite (Fig. 3b). EPMA point analyses show regular variations of major and trace element contents. The dark gray zones are characterized by higher Si, Al, and Mg contents than in light gray zones (Fig. 3c). Vanadium is slightly higher in dark gray zones than light gray zones, whereas Ni contents are similar between different zones (Fig. 3c). Anomalously high

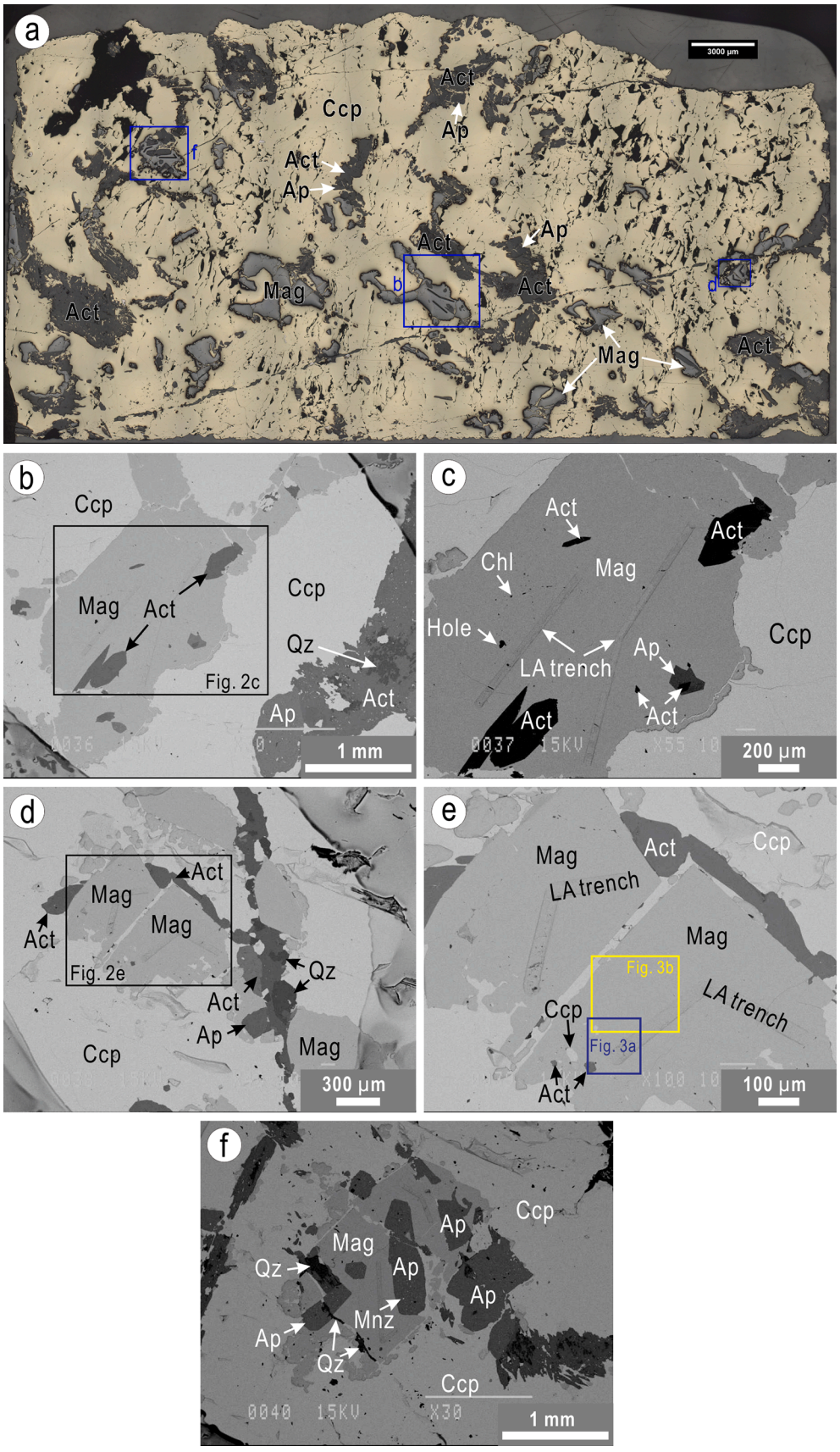

Fig. 2. (a) Reflected light photo of the thin section showing sample 084 composed of mainly chalcopyrite, magnetite, actinolite, and apatite. (b-f) Back-scattered electron (BSE) images of three selected areas in sample 084. In general, mineral assemblages are similar in different areas but with different proportions of minerals. Chalcopyrite is the most abundant. (b-c) Subhedral magnetite is associated with chalcopyrite, actinolite, and apatite. Quartz is locally present. Actinolite, apatite, and minor chlorite occur as inclusions in magnetite. (d-e) Subhedral and anhedral magnetite is associated with actinolite. Apatite and quartz occur as veins crosscutting the massive chalcopyrite. Chalcopyrite and actinolite are the main inclusions in the magnetite. (f) Magnetite and apatite assemblages are cut by later chalcopyrite and quartz veins. Monzonite is widespread in apatite. Shadows in the lower left corner and upper right corner of (b), lower left corner and right margin of (d), are left by colored pens. Abbreviations: Act-actinolite; Ap-apatite; Ccp-chalcopyrite; Chl-chlorite; Mag-magnetite; Qz-quartz.

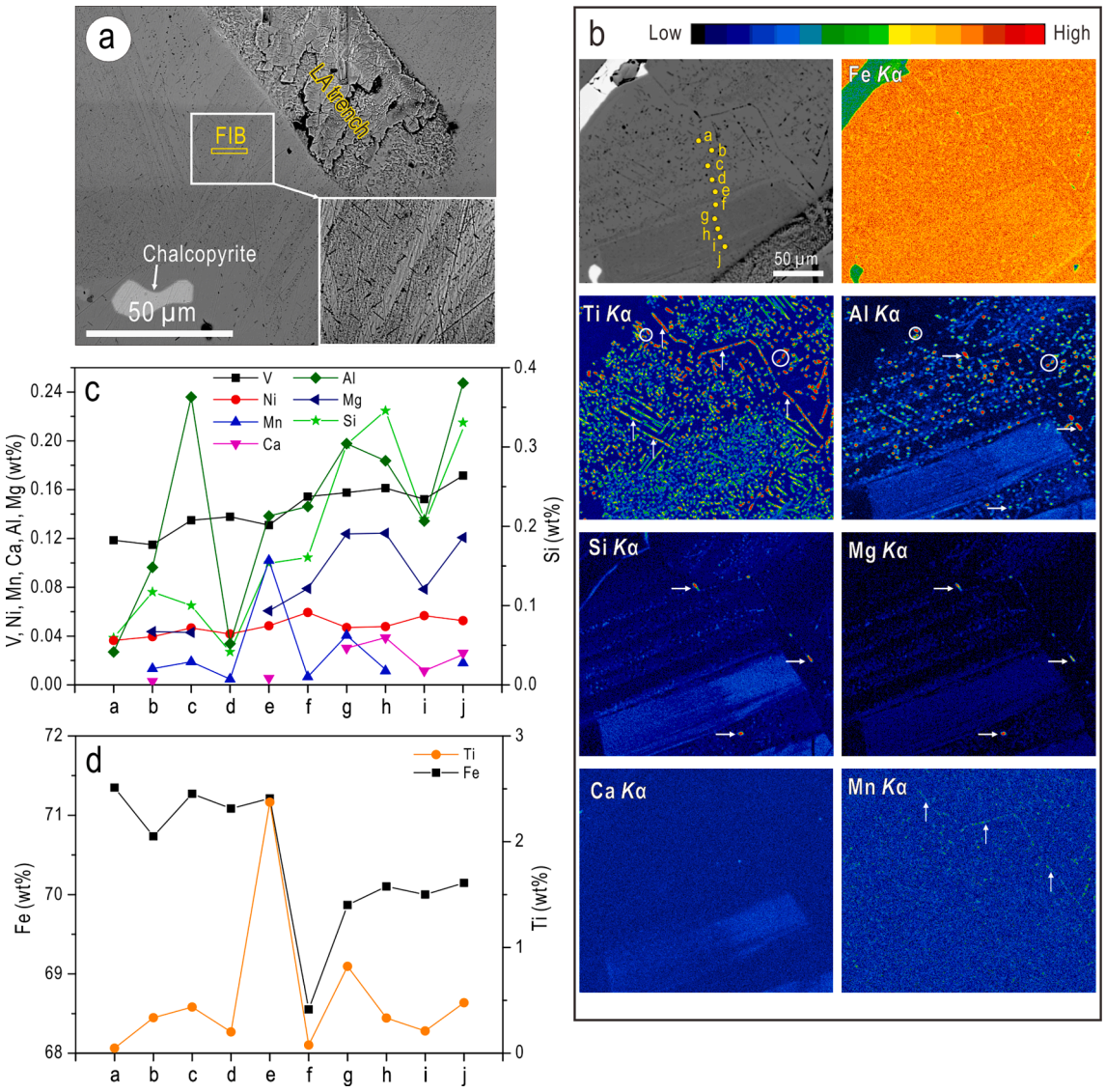

Fig. 3. (a) High-contrast BSE image of a selected area in the studied magnetite grain showing alternative dark gray and light gray zones that form oscillatory zoning. Focused Ion Beam (FIB) crosscuts the dark gray and light gray zones of oscillatory zoning. Image in the lower right corner represents an enlarged view of the rectangular area. (b) BSE image and WDS X-ray maps of a selected area in the studied magnetite grain. There is a similar distribution pattern of Al, Si, and Mg between dark gray and light gray zones. Calcium content in the dark gray zone of magnetite is higher than the light gray zone. Iron and Mn contents are indistinguishable between dark gray and light gray zones. Ilmenite/ulvöspinel occurs as granular inclusions or exsolution lamellae (upward white arrow). Amounts of hercynite inclusions in both dark gray and light gray zones are indicated by high Ti and Al contents (white circle), whereas silicate inclusions are indicated by high Al, Si, and Mg contents (rightward white arrow). (c-d) Variations of major and trace element contents in oscillatory zoning. Silicon, Al, and Mg contents are higher in dark gray zones (location e, g, h, and j) than light gray zones (location a, b, c, d, f, and i). Vanadium content in dark gray zones is slightly higher than light gray zones, whereas Ni contents in both zones are similar. The abrupt increased Al content in location c and Ti contents in location e are possibly due to respective hercynite and ilmenite inclusions. The abrupt decreased Fe, Ti, and Mn contents in location f are due to lack of Fe-Ti oxide inclusions.

Al, Mn, and Ti contents for some points are possibly due to undetected hercynite and Fe-Ti oxide inclusions under the analytical surface (Fig. 3c, d).

The EPMA point analyses show that dark gray zones have higher average Cr, Mn, K, Ca, Ti, Al, Si, and Mg contents than light gray zones (Fig. 4). Vanadium and Ni contents are similar between dark and light gray zones. The dark gray zones have Ti, Al, Si and Mg contents of 0.33–2.37 wt%, 0.11–0.27 wt%, 0.15–0.65 wt%, and 0.06–0.18 wt%, respectively, whereas the light gray zones contain 0.05–0.85 wt% Ti, 0.02–0.55 wt% Al, 0.04–0.41 wt% Si and 0.01–0.14 wt% Mg (Appendix A). There are negative correlations of Fe^{3+} with Si, Ti, and Mg for both dark gray and light gray zones (Fig. 5a, b, d). A weakly negative correlation between V and Fe^{3+} is identified for the light gray zones (Fig. 5c). There is a positive correlation between Fe^{2+} and Si for the light gray zones (Fig. 5e). Manganese and Ti in both dark gray and light gray zones show positive correlations with Fe^{2+} (Fig. 5f, g). Aluminum shows positive correlations with Si and Mg for dark gray zones (Fig. 5h, l). Positive correlations between Si ang Mg, Si and Ca, and Ti and Mn are identified for both dark gray and light gray zones (Fig. 5i-k).

4.2. TEM characterization of nanoinclusions in zoned magnetite

A TEM foil crosscutting magnetite compositional zoning is used to characterize nanoinclusions in magnetite. The HAADF image of the TEM foil shows nanoinclusion-rich zones, separated by zones poor in inclusions (Figs. 6, 7a, 8a). TEM-EDS mapping of selected areas that span inclusion-rich and inclusion-poor zones shows that there is no sharp compositional boundary between these zones from element maps

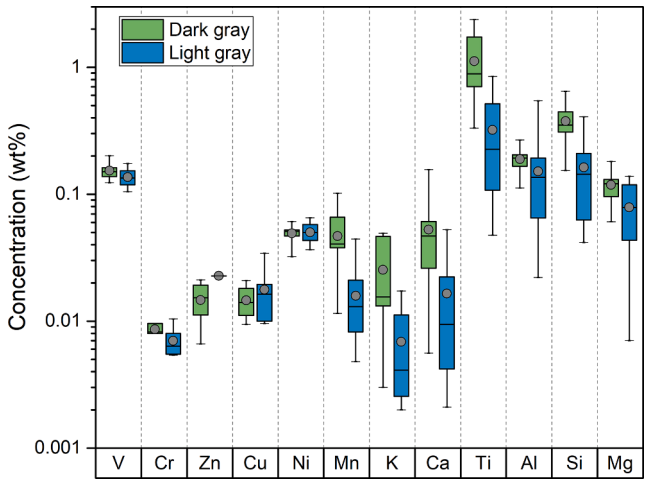

Fig. 4. Box and whisker plots showing the compositional differences between dark gray and light gray zones of magnetite. Boxes outline the 25th to 75th percentiles, and whiskers extend to the minimum and maximum values. Short lines within the box and circles filled by gray on the whiskers represent the median values and average values, respectively. Data are from Huang and Beaudoin (2019) and this study.

(Figs. 7a, 8a, c), in contrast to magnetite zoning from the Los Colorados IOA deposit, which is characterized by sharp changes in relative concentrations of Al, Si, Fe and Ti between zones (Deditius et al., 2018).

The qualitative TEM-EDS mapping and point analyses identify four types of mineral nanoinclusions, in order of abundance: 1) Mg-Fe-(Al)-silicates, most likely amphiboles; 2) Fe-Ti-(Mn-V-bearing) oixde(s), mainly ilmenite; 3) Si-rich magnetite and 4) pyroxene inclusions (Figs. 7–11). Two subgroups of amphiboles are defined based on Ca content and morphology. One group of amphiboles mainly consisting of Si, Mg, Al, and Fe are defined as Mg-Fe amphiboles. Another group of amphiboles composed of Si, Mg, Al, Fe, and minor amounts of Ca are defined as Ca-bearing Mg-Fe amphiboles. Various morphologies and compositions are also observed within the amphibole subgroups. Mg-Fe amphiboles are generally bleb-like, cubic, or hexagonal inclusions disseminated in magnetite matrix, with a size of <~200 × 270 nm (Figs. 7a, 8a, c). Ca-bearing Mg-Fe amphiboles are commonly prismatic, and are orientated parallel to the contact between inclusion-rich and inclusion-poor zones (Fig. 7a). Aluminum in Mg-Fe amphiboles shows a large variation, compared to relatively constant Al in Ca-bearing Mg-Fe amphiboles (Figs. 7b, 8b). Mg-Fe amphiboles and Ca-bearing Mg-Fe amphiboles are separated in magnetite matrix (Fig. 7a) or occur as mineral intergrowths (Fig. 9a). TEM-EDS maps show that both groups of amphiboles occur as an association overprinting Fe-Ti oxide (Figs. 8a, c, 10a, d), resulting in mixed energy-dispersive X-ray signals of amphibole and Fe-Ti oxide (Figs. 8b, 10e). One Ca-bearing Mg-Fe amphibole shows a sharp contact with the host magnetite and has a different crystal structure from the host magnetite (Fig. 10b, c). FFT pattern of the Ca-bearing Mg-Fe amphibole corresponds a zone axis of [1–10] (Fig. 10c).

Two types of Fe-Ti oxide nanoinclusions are identified in the studied magnetite foil: one is prismatic crystal (~2 μm × 150 nm in size) and spans both inclusion-rich and inclusion-poor zones (Fig. 8a, c), whereas the other forms leaf-like crystal (~800 × 300 nm in size) that is nearly perpendicular to the contact between inclusion-rich and inclusion-poor zones, but inside the inclusion-rich zone (Fig. 10a, d). Both Fe-Ti oxide inclusions are intergrown with other silicate minerals and have homogenous Fe, Ti, V and Mn contents (Figs. 8a, c, 10d). There is a clear boundary between Fe-Ti oxide and magnetite (Fig. 8e). The Fe-Ti oxide has FFT pattern different from the host magnetite (Fig. 8f). The sandwich-type lamellar habit (Fig. 3a, b), the presence of Mn and V (Figs. 8c, 10d), major element composition (Figs. 8d, 10e; Appendix B) and FFT pattern (Fig. 8e) indicate that these Fe-Ti oxides are most likely ilmenite.

One prismatic pyroxene nanoinclusion has a size of ~ 470 nm × ~130 nm and is perpendicular to the contact between inclusion-rich and inclusion-poor zones (Fig. 7a, c). Bright-field, low-magnification TEM image shows that the pyroxene has a clear contact with the host magnetite (Fig. 7d) and a crystal structure different from the host magnetite (Fig. 7e). The chemical composition and FFT pattern indicate that pyroxene nanoinclusion is probably pigeonite. Si-rich magnetite nanoinclusion is locally identified in the inclusion-rich zone (Figs. 8a, f and 11). In most cases, magnetite matrix in both inclusion-rich and inclusion-poor zones is close to pure magnetite without detectable impurities (Fig. 7c). Magnetite matrix in some area of the inclusion-rich zone also contains minor to trace Si, K, Al, and Ti (Fig. 9b, c). Bright-field TEM image and FFT patterns indicate epitaxial relationship between Si-rich magnetite nanoinclusion and the host magnetite (Fig. 11a, b).

5. Discussion

5.1. Substitution of trace elements in magnetite

A set of trace elements can be incorporated into magnetite by simple substitution or by coupled substitution. Based on the Goldschmidt's rule, Mg, Mn, Zn, Co, and Ni can substitute for Fe^{2+} in the octahedral sites and Al, Ga, Cr, and As can substitute for Fe^{3+} in the tetrahedral or octahedral sites (Deer et al., 1992; Dupuis and Beaudoin, 2011; Nadoll et al., 2014).

Elements such as Si, Ca, Na, and K are commonly incompatible in magnetite due to large differences (exceeding ± 15–18% variations) in cation radius and charge compared to Fe^{2+} and Fe^{3+} (Goldschmidt, 1958; Dare et al., 2012). The K contents in magnetite measured by EPMA are up to 0.05 wt% (Appendix A), and one Si-rich magnetite matrix contains 0.93 wt% K (Appendix B). No K-bearing nanoinclusions are observed in the studied magnetite, indicating that up to ~ 1 wt% K can be structurally bonded in magnetite. Light gray zones poor in nanoinclusions contain 0.04–0.41 wt% Si (Appendix A). TEM-EDS analyses show that the magnetite matrix in inclusion-poor zone has a chemical composition close to pure magnetite (Fig. 7a, c). It is inferred that Si is lattice-substituted in magnetite of light gray zones. The positive correlation between Fe^{2+} and Si and negative correlation between Fe^{3+} and Si for light gray zones (Fig. 5a, e), probably indicates a coupled substitution, such as $2Fe^{3+} = Si^{4+} + Fe^{2+}$. TEM-EDS analyses show that the magnetite matrix in inclusion-rich zone (Figs. 8a, d and 9b, c) contains up to 7 wt% Si (Appendix B). This Si-rich magnetite matrix in the inclusion-rich zone indicates that Si substitutes into the crystal lattice of magnetite (Westendorp et al., 1991; Shimazaki, 1998; Ohkawa et al., 2007; Huberty et al., 2012; Xu et al., 2014). The lack of correlation of Si with Fe^{2+} and Fe^{3+} for dark gray zones (Fig. 5a, e) is consistent with the main occurrence of Si as silicate nanoinclusions, in addition to minor lattice substitution.

The dark gray zones of the Sossego magnetite contains < 0.16 wt% Ca and < 0.18 wt% Mg (Appendix A), and the magnetite matrix in the inclusion-rich zones has Ca and Mg contents below detection limit (Appendix B), indicating that the measured Ca and Mg contents by EPMA mainly result from Ca-Mg-bearing silicate nanoinclusions. The positive correlations among Si, Ca, Mg, and Al in dark gray zones (Fig. 5h-j, l) thus cannot be interpreted as lattice substitution but silicate nanoinclusions.

EPMA element maps of magnetite show that Mn is homogenously distributed except for some Mn-rich grains and veins (Fig. 3b). The Mn-rich grains are also rich in Ti, indicating that Ti minerals are the main host of Mn. This is consistent with the TEM-EDS maps showing that Mn is relatively enriched in ilmenite compared to its host magnetite (Figs. 8c and 10d). The relatively low Mn contents in zoned magnetite (from below detection limits to 0.1 wt%) and homogenous distribution of Mn in both inclusion-rich and inclusion-poor zones suggest that Mn occurs in magnetite mainly by lattice substitution, in addition to subordinate

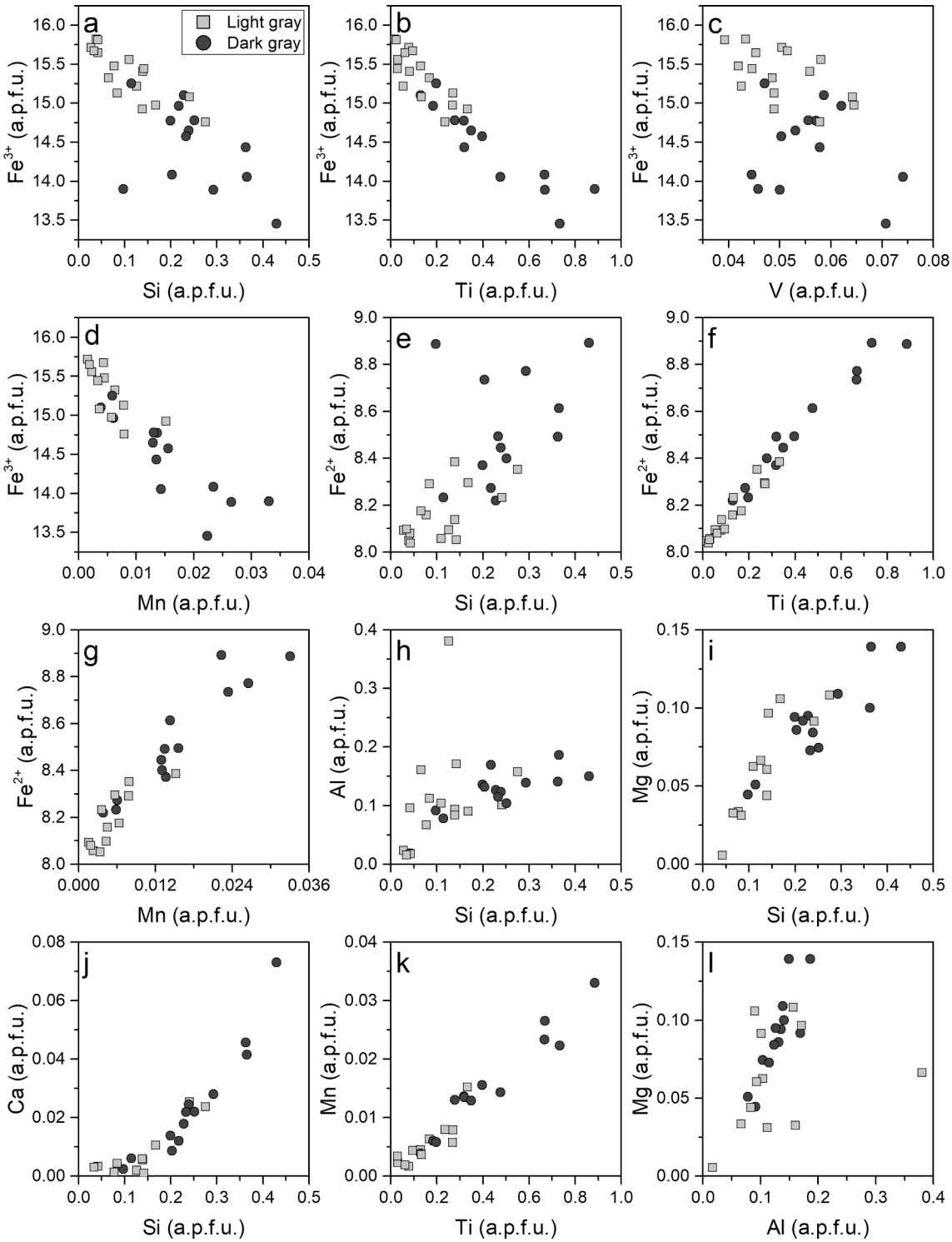

Fig. 5. Binary plots showing the correlation of calculated Fe^{3+} in atom per formula unit (a.p.f.u.) with Si, Ti, V and Mn (a-d), correlation of Fe^{2+} (a.p.f.u.) with Si, Ti, and Mn (e-g), and Si vs. Al, Mg, Ca (h-j), Ti vs. Mn (k), Al vs. Mg (l).

ilmenite nanoinclusions. This is consistent with a good correlation between Mn and Fe^{3+} or Fe^{2+} (Fig. 5d, g).

Titanium distribution in magnetite is heterogeneous (0.05–2.4 wt%), with 0.33–2.37 wt% Ti in inclusion-rich zone (Appendix A). TEM-EDS analyses show that Ti contents in matrix magnetite from both inclusion-rich and inclusion-poor zones are below the detection limit (Appendix B). This indicates that Ti measured by EPMA in magnetite mainly results from ilmenite nanoinclusions (Figs. 8 and 10) rather than solid solution through coupled substitution (Bosi et al., 2009). Therefore, interpretation of the correlation between Ti and Fe^{3+} or Fe^{2+} (Fig. 5b, f) as evidence of lattice substitution should be made with caution in the absence of high-resolution BSE imaging and TEM characterization.

Vanadium has multiple valences (V^{3+}, V^{4+}, and V^{5+}) in silicate melts, and its partition into titanomagnetite crystallized from silicate melt is largely controlled by oxygen fugacity (Toplis and Corgne, 2002; Righter et al., 2006; Sievwright et al., 2017, 2020; Sossi et al., 2018). The relatively low and constant V contents (0.11–0.17 wt%) in zoned

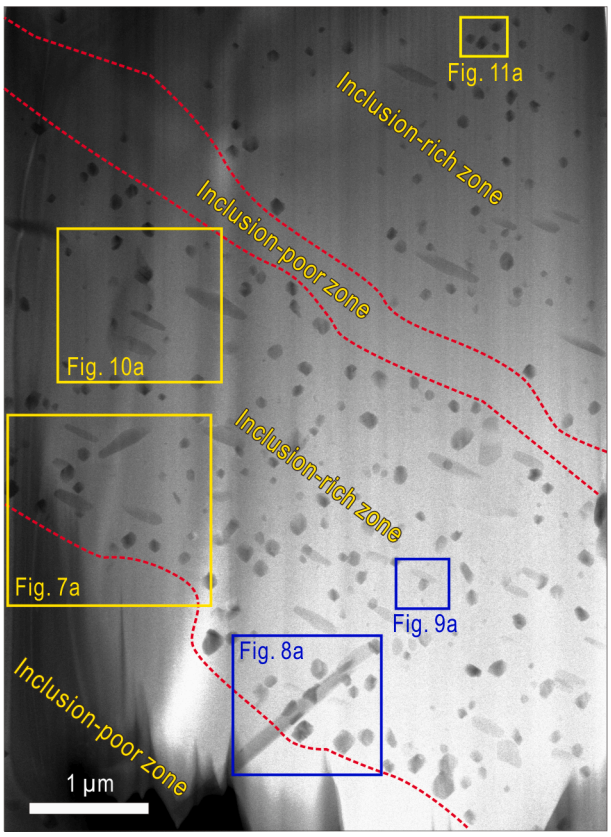

Fig. 6. HAADF images of magnetite foil (~6.8 × 5 μm) prepared by FIB milling. The boundaries between inclusion-rich and inclusion-poor zones are marked by red dotted lines. The areas for TEM-EDS mapping are marked by rectangle. Note that no porosity is observed in magnetite and most of minerals are disseminated in magnetite. Some larger minerals are paralleled to or perpendicular to the boundaries between inclusion-rich and inclusion-poor zones. Different gray levels are caused by differences in thicknesses of the foil.

magnetite from the Sossego deposit indicate relatively stable oxygen fugacity during V incorporation into the magnetite lattice. Vanadium is mainly partitioned into ilmenite where V is homogenously distributed at nm scale (Figs. 8c, 10d), which is consistent with titanomagnetite being the main host for V in the silicate-oxide-sulfide assemblages (Gao et al., 2019).

5.2. Formation of the micron to nanometer inclusions

Petrographic studies using optical microscopy and EPMA identify inclusions of actinolite, apatite, chlorite, chalcopyrite, Fe-Ti oxides, and Ca-Mg-Al silicates in magnetite grains (Figs. 2, 3). These silicate, oxide and chalcopyrite micron-scale inclusions in magnetite are related to high-temperature calcic-iron hydrothermal alteration, based on mineral assemblages (Huang et al., 2019a). Texture indicates that Fe-Ti oxides are exsolution products during magnetite crystallization (Fig. 3b; Huang and Beaudoin, 2019). Actinolite, apatite, chlorite and chalcopyrite have not been detected in the studied magnetite foil by TEM. The most common Ca-poor Fe-Mg amphibole nanoinclusions in magnetite are absent in the mineral assemblage associated with magnetite at macro to micron scales. The various mineral assemblages at different scales for the same sample likely indicates different processes responsible for their formation.

Ilmenite is the dominant Fe-Ti oxide occurring as nanoinclusions in the Sossego magnetite, similar to common spinel and ilmenite in magmatic magnetite (Ciobanu and Cook, 2004; Tan et al., 2016; Gao et al., 2019). Four mechanisms have been proposed for the exsolution of different types of ilmenite from Ti-rich magnetite (Tan et al., 2016). These include exsolution-oxidization or oxy-exsolution of ulvöspinel, direct non-redox exsolution from cation-deficient solid solution, and inter-oxide re-equilibrium (Tan et al., 2016). Different exsolution mechanisms can be distinguished by crystal structure relationship between ilmenite and the host magnetite (Gao et al., 2019). TEM-EDS analyses show that the host magnetite has V content below the detection limit (Appendix B). Lack of intergrowths between V-rich magnetite and ilmenite with 2-fold superstructure indicates that non-redox re-equilibration is probably not the way for ilmenite exsolution in Sossego magnetite (Gao et al., 2019). Alternatively, sandwich-type ilmenite lamellae (Fig. 3a, b) likely result from oxy-exsolution of ulvöspinel from the host magnetite (Tan et al., 2016). Experiments on synthetic and natural Fe-Ti oxides show that ulvöspinel can exsolve from Ti-rich magnetite at about 600 °C and the solvus temperature will be 100 °C lower in the presence of impurities of Al, Mg, Mn, V, and Cr in Ti-rich magnetite (Buddington and Lindsley, 1964; Price, 1981b; Von Gruenewaldt et al., 1985). The exsolution of ulvöspinel results from the miscibility gap between magnetite-ulvöspinel solid solution series (Lindsley, 1981; Price, 1981a). Considering that significant amounts of Mg, Mn, Al, and Si in Ti-rich magnetite, ulvöspinel exsolution from a melt and sequent oxidation to form ilmenite nanoinclusions in the Sossego magnetite may occur at a lower temperature (e.g., ~500 °C). The estimated temperature for ilmenite is consistent with the calculated temperature of 550 ± 25 °C for actinolite-magnetite pair (Monteiro et al., 2008a).

Mg-Fe amphibole and Ca-bearing Mg-Fe amphibole nanoinclusions are common in inclusion-rich magnetite. The close association between Mg-Fe amphibole and Ca-bearing Mg-Fe amphibole (Fig. 9) indicates that amphiboles with different composition and morphologies form simultaneously. The euhedral crystals of these amphibole nanoinclusions indicate that their formation is contemporaneous with the host magnetite. The regular orientation of both groups of amphiboles relative to the host magnetite indicates that they follow the growth of the magnetite crystal. The crosscutting relationship between amphiboles and Fe-Ti oxides (Figs. 8a, 10d) suggests their simultaneous crystallization or slightly later formation of amphiboles. However, the distribution of amphiboles is different from that of Fe-Ti oxides. Amphiboles occur only in the inclusion-rich zone, whereas Fe-Ti oxides are present in both inclusion-rich and inclusion-poor zones (Figs. 3a, b, 8a). Therefore, an exsolution mechanism for ilmenite due to melt/fluid cooling and increased oxygen fugacity cannot be used for the crystallization of amphiboles. Considering the zoned distribution of amphibole nanoinclusions in a single magnetite grain, it can be inferred that amphibole nanoinclusions were precipitated due to local supersaturation in the hydrothermal fluid boundary layer during crystal growth of magnetite (Watson, 1996; Deditius et al., 2018). Most amphibole nanoinclusions are Ca-poor, likely because Ca in the hydrothermal fluid was partitioned into Ca-rich minerals such as actinolite and apatite, and thus magnetite and its nanometer inclusions coprecipitated with these Ca-rich minerals is depleted in Ca. Pigeonite is one of important ferromagnesium silicate minerals in volcanic rocks (Kuno, 1969). These Fe-rich silicate minerals can form at the early stage of basaltic magma fractionation, and also occur as Ca-poor assemblages in the late stage (Kuno, 1969). The pigeonite-bearing andesite dykes near Asio of Japan are interpreted to have formed from late stage of magma with unusually high Fe/Mg ratios (Kuno, 1969). The existence of these Fe-rich minerals such as pigeonite and amphibole in magnetite matrix further indicates that these ferromagnesium silicate minerals together with magnetite probably formed at a relatively high temperature at magmatic condition or magmatic-hydrothermal transitional condition.

Si-rich magnetite, characterized by relatively high Si contents of 6.35–7.71 wt% (Appendix B), has been found as a single nanoinclusion or magnetite matrix in inclusion-rich zone. In some cases, Si-rich magnetite also contains detectable Al, K, and Ti, similar to Si-Fe nanoinclusions in magnetite from the Olympic Dam deposit, South Australia

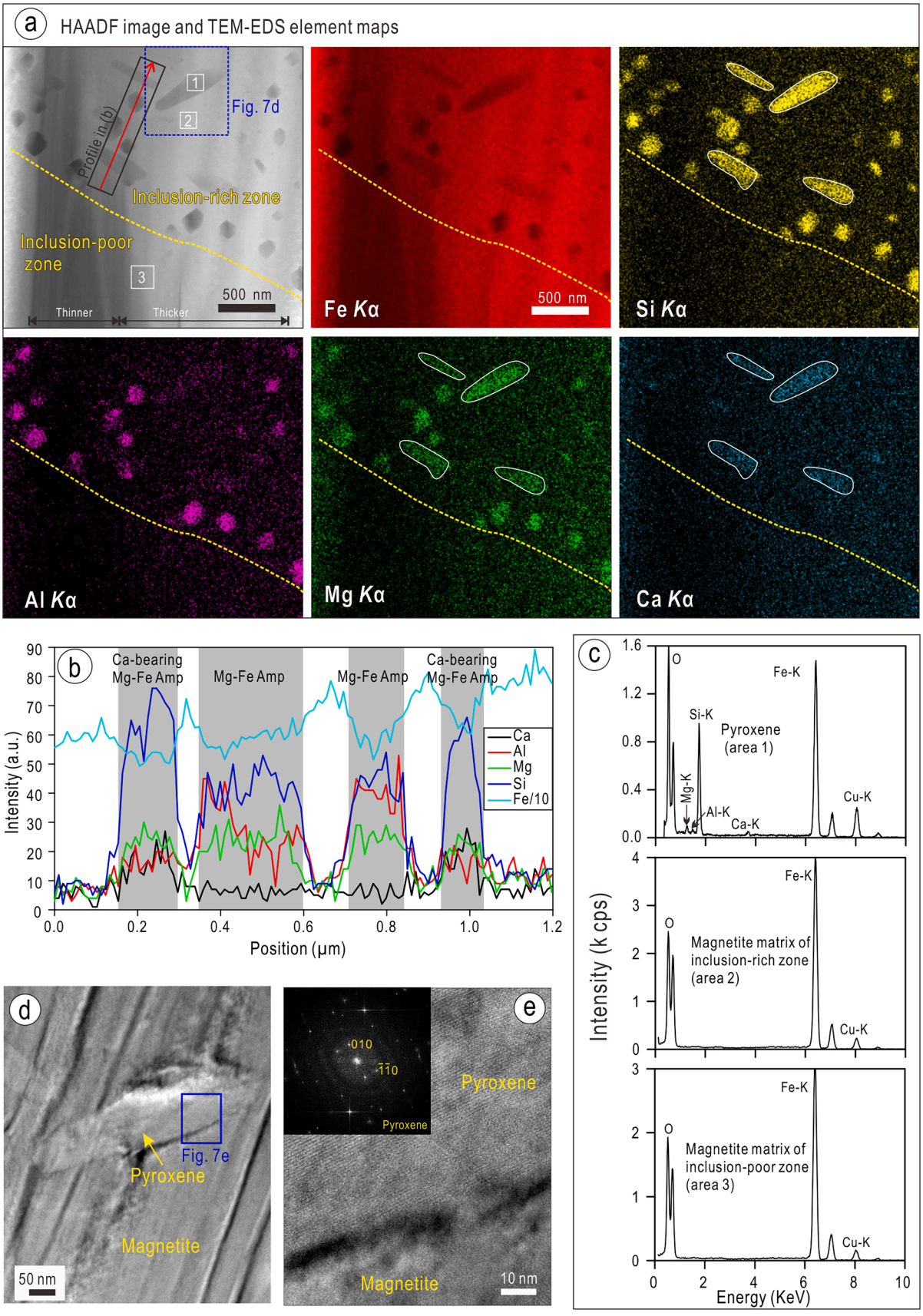

(caption on next page)

Fig. 7. (a) HAADF image and TEM-EDS element maps showing magnetite composed of the inclusion-rich and inclusion-poor zones. There are no obvious differences in Fe, Si, Al, Mg, and Ca contents between inclusion-rich and inclusion-poor zones. Inclusion-rich zone contains larger, prismatic Fe-Si-Ca-Mg (marked by white lines) and cubic Fe-Si-Al-Mg nanoinclusions. The variations in gray scale in HAADF image can be partly explained by differences in the thickness of magnetite foil rather than the differences in composition. (b) A profile in the inclusion-rich zone marked in (a) showing variation of element counts (in atom unit) that indicates the occurrence of Ca-bearing Mg-Fe amphiboles and Mg-Fe amphiboles. Aluminum intensity is various between Mg-Fe amphiboles. (c) Spectra of pyroxene, and magnetite matrix of inclusion-rich and inclusion-poor zones from areas marked in (a). (d) Bright-field, low-magnification TEM images of nanometer minerals in magnetite. (e) HRTEM images of the grain boundary between pyroxene and the host magnetite. Insets in (e) is FFT pattern of pyroxene transformed from HRTEM image. Abbreviation: Amp-amphibole.

(Ciobanu et al., 2019). FFT patterns show that Si-rich magnetite follows the crystal structure of the host magnetite (Fig. 11a, b). The Si-rich magnetite nanoparticles can exsolve from the host silician magnetite at low temperature due to the minimization of interfacial energy between the nanoparticles and the host magnetite (Xu et al., 2014), or precipitate from hydrothermal fluids containing Si- and Fe complexes (Ciobanu et al., 2019).

5.3. Formation of oscillatory zoning

Oscillatory zoning in magmatic and hydrothermal minerals is a common texture that can be formed by both internal crystal growth and external changes in conditions such as melt/fluid composition, temperature, and pressure (Shore and Fowler, 1996; Holten et al., 2000). Oscillatory zoned magnetite has been documented in Fe skarn (Shimazaki, 1998; Ciobanu and Cook, 2004; Dare et al., 2014; Huang et al., 2018), IOCG (Huang and Beaudoin, 2019), and IOA (Knipping et al., 2015; Deditius et al., 2018) deposits, as well as some replaced lava flows (Dare et al., 2015) and altered phreatomagmatic pipes (Neumann et al., 2017). Two main mechanisms are used to explain the formation of oscillatory zoning in magnetite. Some consider that oscillatory zoning is a self-organized texture similar to Liesegang banding (Putnis et al., 1992) due to internal, near-equilibrium crystal growth (Ortoleva et al., 1987; Hjelmfelt and Ross, 1991; Ciobanu and Cook, 2004; Neumann et al., 2017), whereas others argue that cyclical fluctuations in external factors such as pressure, temperature, or fluid composition are responsible for the formation of oscillatory zoning (Shimazaki, 1998; Dare et al., 2015; Knipping et al., 2015; Huang et al., 2018).

EPMA analyses show that inclusion-rich zones have higher Al, Si, Ca, Mg, and Ti contents than the inclusion-poor zones (Figs. 3c, d and 4), which are mainly due to the proportion of nm-scale silicate and Fe-Ti oxide inclusions in inclusion-rich zones (Fig. 6). Titanium content in magnetite, an indicator for temperature in magmatic and hydrothermal systems (Nielsen et al., 1994; Nadoll et al., 2014; Sievwright et al., 2017), shows no significant differences between inclusion-rich and inclusion-poor zones at the nm-scale (Fig. 8c), implying that variation in temperature is not an important factor for the formation of chemical zoning. The limited variations of V contents (0.11–0.17 wt%) between inclusion-rich and inclusion-poor zones are consistent with the relative constant oxygen fugacity during zonation formation, similar to the observation for zoned magnetite from the Los Colorados IOA deposit (Deditius et al., 2018). Therefore, oscillatory zoning must have formed under relatively constant temperature and oxygen fugacity.

The presence of sector or oscillatory zoning is commonly viewed as evidence for surface enrichment where disequilibrium uptake of minor and trace elements (growth entrapment) will occur when the rate of crystal growth is higher than that of lattice diffusion (Watson and Liang, 1995; Watson, 1996). The relation between growth entrapment and temperature indicates that growth entrapment is expected to happen when surface enrichment occurs at a temperature below ~ 700 °C, whereas growth entrapment is unlikely in minerals crystallized from melts above ~ 1000 °C (Watson, 1996). This explains why oscillatory zoning is present in both the magmatic magnetite from diorite intrusions (Knipping et al., 2015) and magmatic-hydrothermal magnetite from IOCG, IOA and skarn Fe-Cu deposits (Ciobanu and Cook, 2004; Deditius et al., 2018; Huang and Beaudoin, 2019).

The existence of Si-rich magnetite and silicate nanoinclusions in inclusion-rich zones suggests mineral supersaturation in the inclusion-rich zone. Supersaturation of oxide and silicate minerals results in the depletion of Si, Ca, Al, and Mg in the boundary layer fluids and formation of inclusion-poor magnetite, depleted or with low contents of these elements. This process repeats during magnetite crystallization and results in the formation of zoned magnetite. Supersaturation of minerals can be due to fluid-magnetite reaction via interfacial dissolution and reprecipitation mechanism during non-equilibrium crystal growth of magnetite (Yardley et al., 1991; Yin et al., 2017, 2019). However, this model cannot be used to explain the formation of oscillatory zoning in the studied magnetite, because of absence of typical features of dissolution and reprecipitation such as pervasive porosity and sharp reaction front at both the micron and nanometer scale (Putnis and Austrheim, 2013). Calcite growth experiments have demonstrated that the oscillatory zoning in calcite is not consistent with external perturbations such as variation in fluid compositions (Reeder et al., 1990). The relatively stable temperature and oxygen fugacity conditions at Sossego precludes major control of external factors on the formation of oscillatory zoning in magnetite. Therefore, we suggest that oscillatory zoning in magnetite from the Sossego deposit represents an example of self-organization where fluctuations in chemical compositions resulted from autonomous response of an evolving fluid system far from equilibrium.

5.4. Implication for the discrimination of magnetite source using chemical composition

Major and trace element compositions of magnetite have been used to discriminate different types of mineral deposits or magmatic and hydrothermal magnetite (e.g., Dupuis and Beaudoin, 2011; Dare et al., 2014; Nadoll et al., 2014; Huang et al., 2019a, Huang et al., 2019b). As shown in Fig. 12, analyses from the sample 084 show a large variation with Ca + Al + Mn contents ranging from < 0.01 to 0.55 wt% and Ti + V contents from 0.16 to 2.50 wt%. Moreover, analyses from a single grain of zoned magnetite (084C and 084D) also display similar variations. The considerable compositional variation mainly results from the irregular distribution of nanoinclusions in magnetite. Two types of ilmenite nanoinclusions and a large number of silicate nanoinclusions are found in ~ 7 × 5 μm magnetite foil. It is thus unavoidable to analyze these nanoinclusions in magnetite using μm scale beam size of EPMA (1–10 μm) and LA-ICP-MS (20–100 μm). It can be inferred that Ti + V contents in magnetite will increase due to analyses of Fe-Ti oxide (e.g., ilmenite) nanoinclusions, whereas Ca + Al + Mn contents will increase due to analyses of silicate or Al-bearing spinel nanoinclusions (Fig. 12). There is some advantage to using an electron or laser beam larger than the size of the nanoinclusions formed by exsolution, because this will yield the composition of the mineral before the exsolution process stopped at some specific temperature and fO_2 conditions, which are those recorded by the composition of the host and exsolved phase (Dare et al. 2012). Therefore, caution should be taken when interpretation the variations in magnetite chemistry considering the heterogeneous distribution of micron- to nanometer-scale inclusions in some magnetite grains.

The existence of nanoinclusions in magnetite complicates the application of related discrimination diagrams, but nano-scale mineral assemblage still can provide some important constraints on the origin of magnetite. Deditius et al. (2018) identified diopside, clinoenstatite, amphibole, mica, ulvöspinel, and Ti-rich magnetite nanoinclusions and ascribed the host zoned magnetite to a hydrothermal origin. Ciobanu

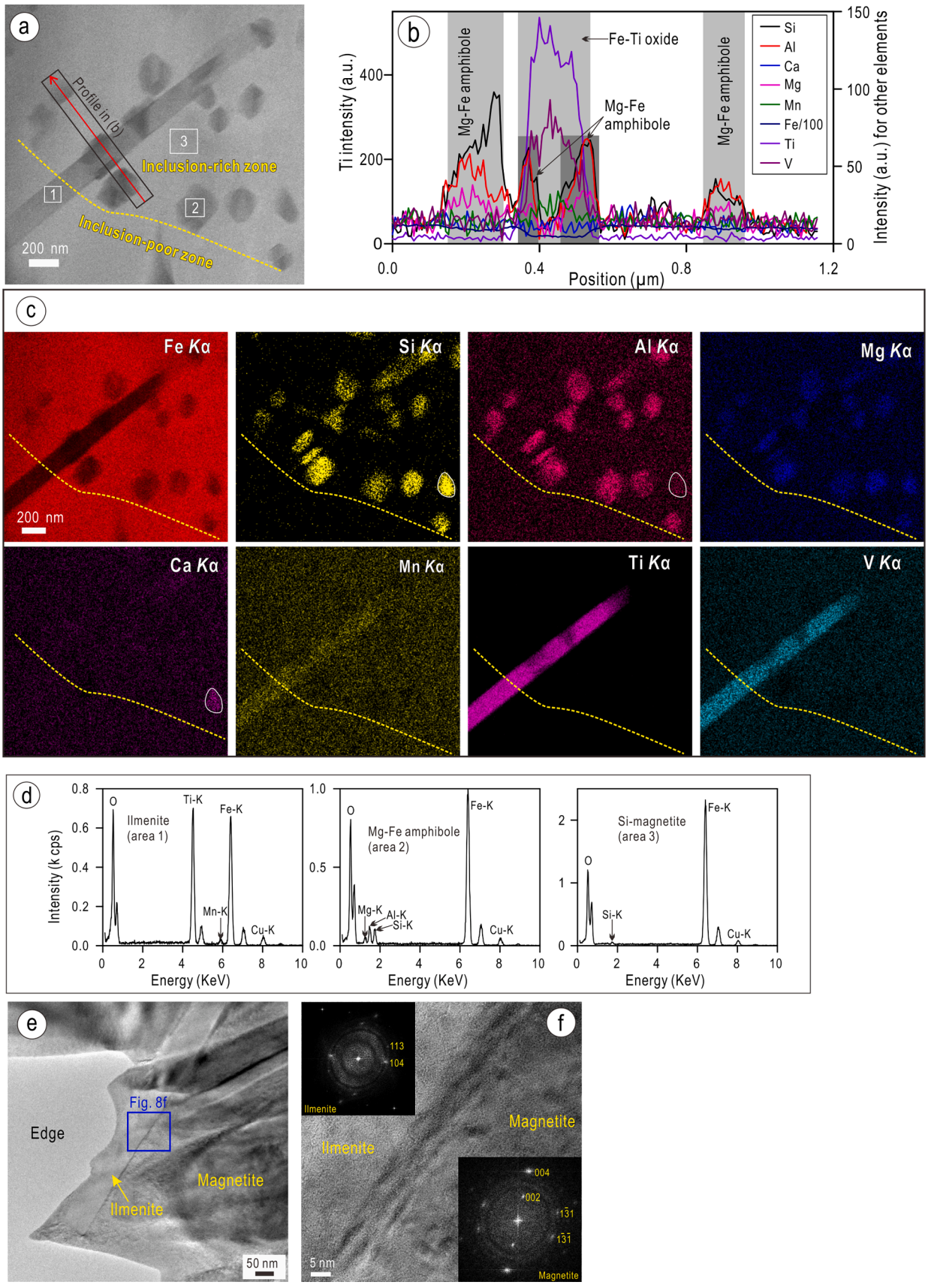

(caption on next page)

Fig. 8. (a) HAADF image showing the types and distribution of mineral nanoinclusions in inclusion-rich and inclusion-poor zones. (b) A profile in the inclusion-rich zone showing the Mg-Fe amphiboles are associated with an Fe-Ti oxide mineral. (c) TEM-EDS element maps of image in a. Note that prismatic Fe-Ti oxide spans the boundary between inclusion-rich and inclusion-poor zones and the long axis of this mineral is nearly perpendicular to the boundary. No obvious differences in Fe, Si, Mg, Al, Mn, Ca, Ti, and V X-ray signals are observed between inclusion-rich and inclusion-poor zones. Fe-Ti oxide nanoinclusions can be identified by relatively high Ti, V, and Mn contents, whereas silicate nanoinclusions are characterized by high Si, Al, and Mg contents. One silicate nanoinclusion (marked with circle) contain more Ca but less Al than other silicates. (d) Spectra of ilmenite, Mg-Fe amphibole, and Si-magnetite from areas marked in (a). (e) Bright-field, low-magnification TEM image showing ilmenite inclusion in magnetite. (f) HRTEM image of the grain boundary between ilmenite and magnetite. Insets in (f) are FFT patterns of minerals transformed from HRTEM images.

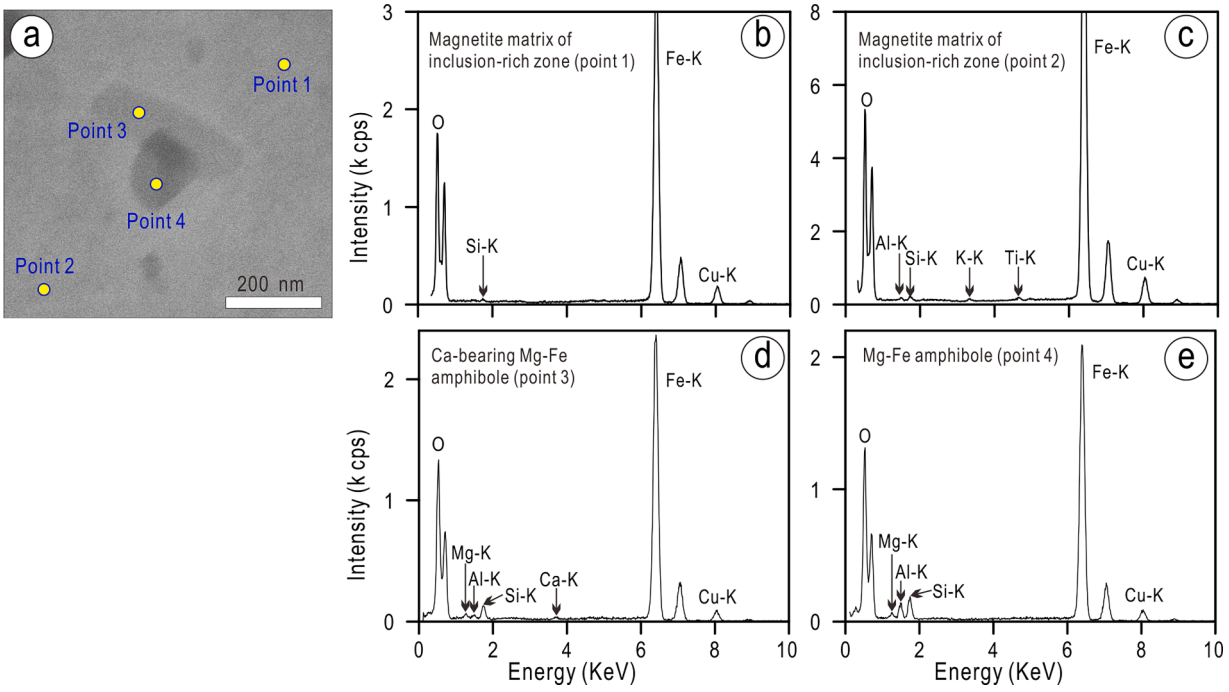

Fig. 9. (a) HAADF image of a selected area in inclusion-rich zone showing the close association of prismatic Ca-bearing Mg-Fe amphibole and cubic Mg-Fe amphibole. (b-c) Spectra of magnetite matrix in inclusion-rich zone that are characterized by detectable Si. (d-e) Spectra of amphibole with different compositions.

et al. (2019) identified magmatic and siliceous nanometer-scale domains of a magnetite grain from the Olympic Dam IOCG deposit. The magmatic domain is characterized by amounts of hercynite and ilmenite nanoinclusions, whereas the siliceous domain contains actinolite, Si-Fe-nanoprecipitates and rutile that are assigned to hydrothermal origin (Ciobanu et al., 2019). Silician magnetite from hydrothermal deposits, particularly porphyry, VMS and skarn deposits, can have Si contents up to 4 wt% (Shcheka et al., 1977; Westendorp et al., 1991; Shimazaki, 1998; Ohkawa et al., 2007; Huberty et al., 2012; Dare et al., 2015; González et al., 2018), whereas those from magmatic deposits contain an average 1.2 wt% Si (Newberry et al., 1982). Considering that Si-rich magnetite nanoinclusions in the Sossego deposit contain up to 7.7 wt% Si and also contain minor amounts of K and Al, we suggest that they have formed from Si-K-Al-rich hydrothermal fluids. Moreover, presence of nanoinclusions of ferromagnesium silicate minerals and ilmenite suggests the formation of host magnetite at a relatively high temperature (e.g., <600–500 °C) that is close to magmatic or magmatic to hydrothermal transitional conditions. The high-temperature magmatic or magmatic-hydrothermal origin of nanoinclusions and the host magnetite is consistent with characteristic mineral assemblages and mineral chemistry of the Sossego deposit (Monteiro et al., 2008b; Huang and Beaudoin, 2019; Huang et al., 2019a). Therefore, the nanoscale mineral assemblage is an important complement for the source discrimination of magnetite.

6. Conclusions

Zoned magnetite from the Sossego IOCG deposit provides an excellent example for the studies on element incorporation and mineral formation during magnetite growth. Trace elements are incorporated into magnetite by solid solution when fluids are undersaturated in most minerals, but nanoinclusions will precipitate along with magnetite crystallization where silicates and oxides are supersaturated in the boundary layer. The mineral nanoinclusions in zoned magnetite explain the heterogeneous distribution of some trace elements at the micron scale. Instantaneous supersaturation results in the formation of silicate and oxide minerals that will yield trace element-rich zones in magnetite, whereas oxy-exsolution of ulvöspinel is responsible for the formation of ilmenite from Ti-rich magnetite. Temperature and oxygen fugacity have little influence on the formation of oscillatory zoning at Sossego. Oscillatory zoning was a crystal growth texture formed by a self-organized process where saturation of silicates causes Si, Ca, Mg, Al, K depletion in boundary layer and formation of inclusion-poor magnetite poor in these elements. In view of pervasive existence of nanoinclusions in magnetite from IOA (Deditius et al., 2018), IOCG (Ciobanu et al., 2019; this study), and skarn (Yin et al., 2019) deposits, the interpretation of in situ (e.g., EPMA and LA-ICP-MS) compositional data should be based on detailed textural characterization. Moreover, nanoscale mineral assemblages can be used to assist discriminating the origin of magnetite. This study also highlights that high-resolution TEM analyses at the nanoscale combined with micron-scale EPMA analyses will provide more precise and detailed crystal-chemical information of minerals, particularly those with complex textures.

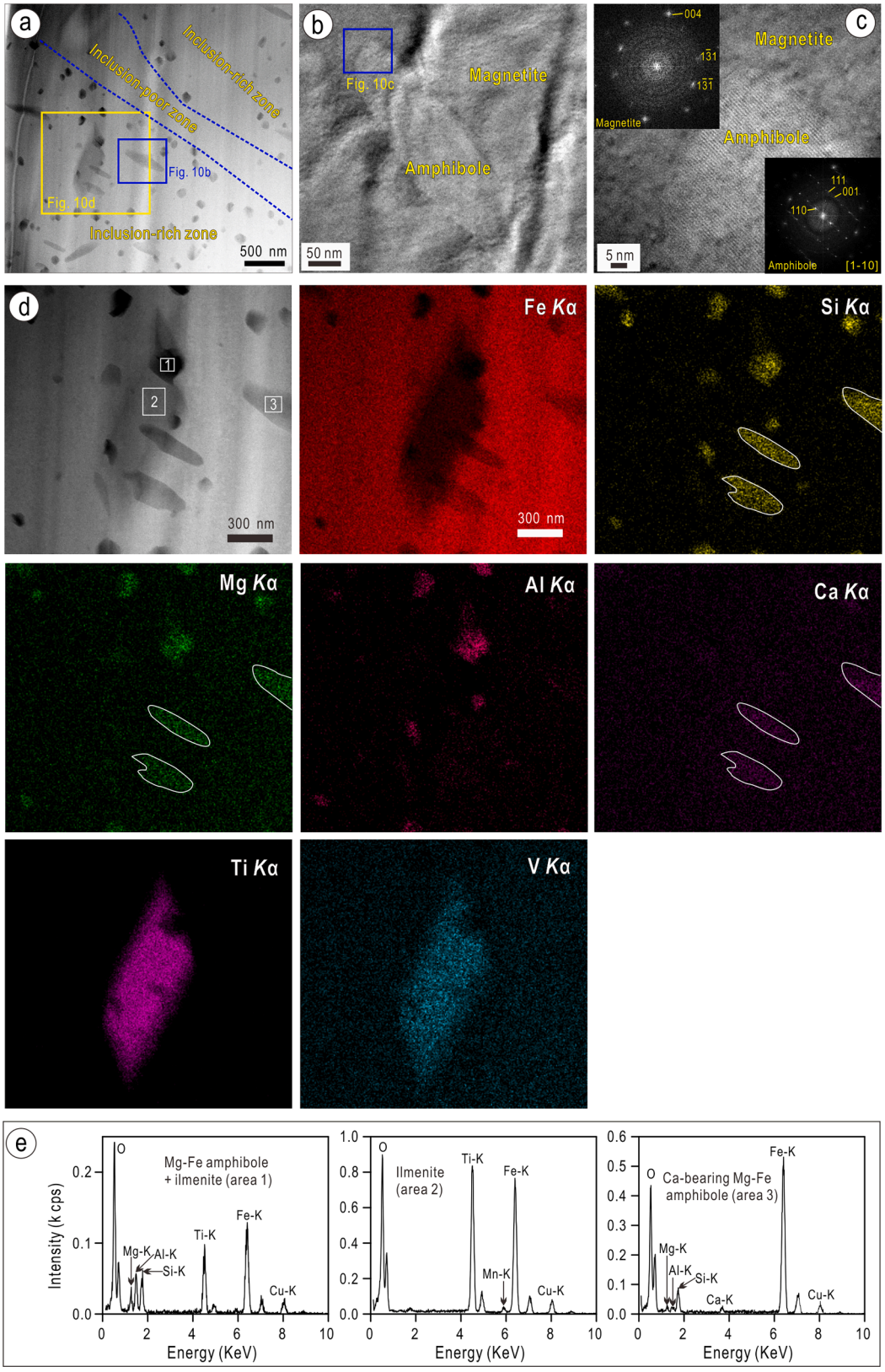

Fig. 10. (a) HAADF image showing alternating inclusion-rich and inclusion-free zones. (b) Bright-field, low-magnification TEM image of selected area in (a). (c) HRTEM image of the grain boundary between amphibole on [1–10] zone axis and the host magnetite. Insets in (c) are FFT patterns of minerals transformed from HRTEM images. (d) HAADF image and TEM-EDS element maps of a selected area in inclusion-rich zone showing amphiboles are closely associated with Fe-Ti oxide. Fe-Ti oxide nanoinclusions (ilmenite) are characterized by high Ti and V signals, whereas silicate nanoinclusions (amphibole with different compositions) can be identified by high Si-Mg-Ca or Si-Mg-Al signals. e Spectra of selected areas marked in (d) indicating ilmenite, the mixture between amphiboles and ilmenite.

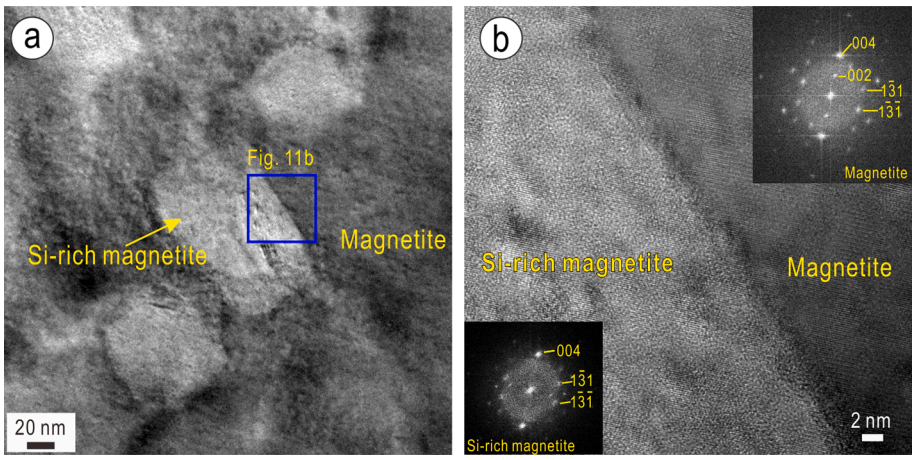

Fig. 11. (a) Bright-field, low-magnification TEM image of a selected area in inclusion-rich zone. (b) HRTEM images of the grain boundary between Si-rich magnetite and the host magnetite. Insets in (b) is FFT pattern of minerals transformed from HRTEM image. Si-rich magnetite shows epitaxial relationship with the host magnetite.

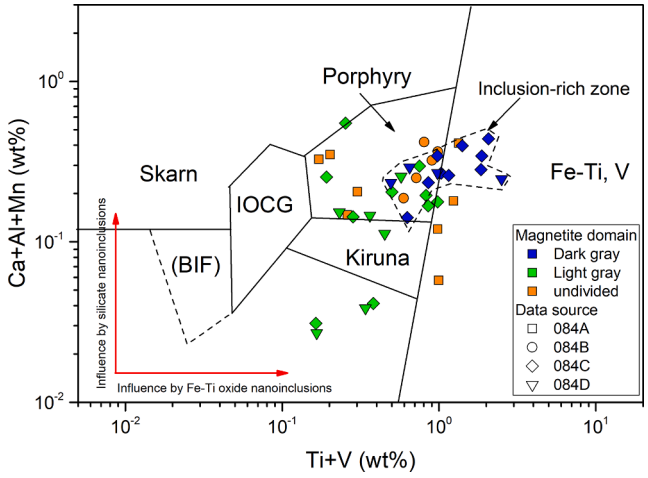

Fig. 12. Plot of Ti + V versus Ca + Al + Mn showing the chemical composition of magnetite from sample 084 of the Sossego IOCG deposit. Note that the occurrence of Fe-Ti oxide nanoinclusions in inclusion-rich zone will increase contents of Ti and V, whereas existence of silicate nanoinclusions will increase Ca, Al, or Mn contents in magnetite. The fields of different deposit types are based on Dupuis and Beaudoin (2011). Abbreviations: BIF-banded iron formation; Skarn-Fe–Cu skarn deposits; IOCG-iron oxide–copper–gold deposits; Porphyry-porphyry Cu deposits; Kiruna-Kiruna apatite–magnetite deposits; Fe–Ti, V-magmatic Fe–Ti–oxide deposits. 084A and 084B represent respective EPMA and LA-ICP-MS analyses from Huang et al. (2019a), whereas 084C and 084D are EPMA data from Huang and Beaudoin (2019) and this study, respectively.

Declaration of Competing Interest

The authors declare that they have no known competing financial interests or personal relationships that could have appeared to influence the work reported in this paper.

Acknowledgments

We thank Marc Choquette (Laval U.) for his assistance with EPMA analyses and Hui Yuan and Natalie Hamada (CCEM) for helping FIB-TEM analyses. Yiping Yang (Guangzhou Institute of Geochemistry, CAS) is thanked for interpreting the HRTEM images. This project was funded by "CAS Hundred Talents Program" project (Y9CJ034000) to XWH, the Natural Sciences and Engineering Research Council (NSERC) of Canada, Agnico Eagle Mines Limited, and Ministère de l'Énergie et des Ressources Naturelles du Québec within the NSERC-Agnico Eagle Industrial Research Chair in Mineral Exploration. The Editors Huayong Chen and Hélène Legros, and anonymous reviewers are thanked for the critical review on the manuscript.

Appendix A. Supplementary data

Supplementary data to this article can be found online at https://doi.org/10.1016/j.oregeorev.2021.104453.

References

Acosta-Gongora, P., Gleeson, S.A., Samson, I.M., Ootes, L., Corriveau, L., 2014. Trace element geochemistry of magnetite and its relationship to Cu-Bi-Co-Au-Ag-U-W mineralization in the Great Bear magmatic zone, NWT, Canada. Econ. Geol. 109 (7), 1901–1928.

Bosi, F., Halenius, U., Skogby, H., 2009. Crystal chemistry of the magnetite-ulvospinel series. Am. Mineral. 94 (1), 181–189.

Broughm, S.G., Hanchar, J.M., Tornos, F., Westhues, A., Attersley, S., 2017. Mineral chemistry of magnetite from magnetite-apatite mineralization and their host rocks: examples from Kiruna, Sweden, and El Laco, Chile. Miner. Deposita 52 (8), 1223–1244.

Buddington, A.F., Lindsley, D.H., 1964. Iron-titanium oxide minerals and synthetic equivalents. J. Petrol. 5 (2), 310–357.

Canil, D., Grondahl, C., Lacourse, T., Pisiak, L.K., 2016. Trace elements in magnetite from porphyry Cu–Mo–Au deposits in British Columbia, Canada. Ore Geol. Rev. 72, 1116–1128.

Canil, D., Lacourse, T., 2020. Geothermometry using minor and trace elements in igneous and hydrothermal magnetite. Chem. Geol. 541, 119576.

Ciobanu, C.L., Cook, N.J., 2004. Skarn textures and a case study: the Ocna de Fier-Dognecea orefield, Banat, Romania. Ore Geol. Rev. 24 (3-4), 315–370.

Ciobanu, C.L., Verdugo-Ihl, M.R., Slattery, A., Cook, N.J., Ehrig, K., Courtney-Davies, L., Wade, B.P., 2019. Silician Magnetite: Si–Fe-nanoprecipitates and other mineral inclusions in magnetite from the Olympic dam deposit, South Australia. Minerals 9 (5), 311. https://doi.org/10.3390/min9050311.

Cook, N., Ciobanu, C.L., George, L., Zhu, Z.-Y., Wade, B., Ehrig, K., 2016. Trace element analysis of minerals in magmatic-hydrothermal ores by laser ablation inductively-coupled plasma mass spectrometry: approaches and opportunities. Minerals 6, 1–34.

Dare, S.A.S., Barnes, S.-J., Beaudoin, G., 2012. Variation in trace element content of magnetite crystallized from a fractionating sulfide liquid, Sudbury, Canada: implications for provenance discrimination. Geochim. Cosmochim. Acta 88, 27–50.

Dare, S.A.S., Barnes, S.-J., Beaudoin, G., Méric, J., Boutroy, E., Potvin-Doucet, C., 2014. Trace elements in magnetite as petrogenetic indicators. Miner. Deposita 49 (7), 785–796.

Dare, S.A.S., Barnes, S.-J., Beaudoin, G., 2015. Did the massive magnetite "lava flows" of El Laco (Chile) form by magmatic or hydrothermal processes? New constraints from magnetite composition by LA-ICP-MS. Miner. Deposita 50 (5), 607–617.

Deditius, A.P., Reich, M., Simon, A.C., Suvorova, A., Knipping, J., Roberts, M.P., Rubanov, S., Dodd, A., Saunders, M., 2018. Nanogeochemistry of hydrothermal magnetite. Contrib. Mineral. Petrol. 173, 46.

Deer, W.A., Howie, R.A., Zussman, J., 1992. An Introduction to the Rock-Forming Minerals, second ed. Longman, Harlow, Wiley, New York.

Dupuis, C., Beaudoin, G., 2011. Discriminant diagrams for iron oxide trace element fingerprinting of mineral deposit types. Miner. Deposita 46 (4), 319–335.

Gao, W., Ciobanu, C.L., Cook, N.J., Slattery, A., Huang, F., Song, D., 2019. Nanoscale study of titanomagnetite from the Panzhihua layered intrusion, Southwest China: multistage exsolutions record ore formation. Minerals 9 (9), 513. https://doi.org/10.3390/min9090513.
Goldschmidt, V.M., 1958. Geochemistry. Oxford University Press, London, pp. 1–730.
González, E., Kojima, S., Ichii, Y., Tanaka, T., Fujimoto, Y., Ogata, T., 2018. Silician Magnetite from the Copiapó Nordeste prospect of northern chile and its implication for ore-forming conditions of iron oxide–copper–gold deposits. Minerals 8 (11), 529.
Gourcerol, B., Kontak, D.J., Thurston, P.C., Duparc, Q., 2016. Do magnetite layers in algoma-type banded iron formations (BIF) preserve their primary geochemical signature? A case study of samples from three Archean BIF-hosted gold deposits. Can. Mineral. 54 (3), 605–624.
Hjelmfelt, A., Ross, J., 1991. Experiments on an oscillatory system close to equilibrium. J. Chem. Phys. 94 (9), 5999–6002.
Holten, T., Jamtveit, B., Meakin, P., 2000. Noise and oscillatory zoning of minerals. Geochim. Cosmochim. Acta 64 (11), 1893–1904.
Huang, X.-W., Beaudoin, G., 2019. Textures and chemical composition of magnetite from iron oxide-copper-gold (IOCG) and Kiruna-type iron oxide-apatite (IOA) deposits and their implications for ore genesis and magnetite classification schemes. Econ. Geol. 114, 953–979.
Huang, X.-W., Sappin, A.-A., Boutroy, É., Beaudoin, G., Makvandi, S., 2019b. Trace element composition of igneous and hydrothermal magnetite from porphyry deposits: Relationship to deposit subtypes and magmatic affinity. Econ. Geol. 114, 917-952.
Huang, X., Qi, L., Meng, Y., 2014. Trace element geochemistry of magnetite from the Fe (-Cu) deposits in the Hami region, Eastern Tianshan Orogenic Belt, NW China. Acta Geol. Sin. 88 (1), 176–195.
Huang, X.-W., Zhou, M.-F., Qi, L., Gao, J.-F., Wang, Y.-W., 2013. Re-Os isotopic ages of pyrite and chemical composition of magnetite from the Cihai magmatic-hydrothermal Fe deposit, NW China. Miner. Deposita 48 (8), 925–946.
Huang, X.-W., Gao, J.-F., Qi, L., Zhou, M.-F., 2015a. In-situ LA-ICP-MS trace elemental analyses of magnetite and Re–Os dating of pyrite: the Tianhu hydrothermally remobilized sedimentary Fe deposit, NW China. Ore Geol. Rev. 65, 900–916.
Huang, X.-W., Zhou, M.-F., Qiu, Y.-Z., Qi, L., 2015b. In-situ LA-ICP-MS trace elemental analyses of magnetite: the Bayan Obo Fe-REE-Nb deposit, North China. Ore Geol. Rev. 65, 884–899.
Huang, X.-W., Gao, J.-F., Qi, L., Meng, Y.-M., Wang, Y.-C., Dai, Z.-H., 2016. In-situ LA-ICP-MS trace elements analysis of magnetite: the Fenghuangshan Cu-Fe-Au deposit, Tongling, Eastern China. Ore Geol. Rev. 72, 746–759.
Huang, X.-W., Zhou, M.-F., Beaudoin, G., Gao, J.-F., Qi, L., Lyu, C., 2018. Origin of the volcanic-hosted Yamansu Fe deposit, Eastern Tianshan, NW China: constraints from pyrite Re-Os isotopes, stable isotopes, and in situ magnetite trace elements. Miner. Deposita 53 (7), 1039–1060.
Huang, X.-W., Boutroy, É., Makvandi, S., Beaudoin, G., Corriveau, L., De Toni, A.F., 2019a. Trace element composition of iron oxides from IOCG and IOA deposits: relationship to hydrothermal alteration and deposit subtypes. Miner. Deposita 54 (4), 525–552.
Huberty, J.M., Konishi, H., Heck, P.R., Fournelle, J.H., Valley, J.W., Xu, H., 2012. Silician magnetite from the Dales Gorge Member of the Brockman Iron Formation, Hamersley Group, Western Australia. Am. Mineral. 97 (1), 26–37.
Jarosewich, E., Nelen, J., Norberg, J.A., 1980. Reference samples for electron microprobe analysis. Geostand. Newslett. 4, 43-47.
Knipping, J.L., Bilenker, L.D., Simon, A.C., Reich, M., Barra, F., Deditius, A.P., Wälle, M., Heinrich, C.A., Holtz, F., Munizaga, R., 2015. Trace elements in magnetite from massive iron oxide-apatite deposits indicate a combined formation by igneous and magmatic-hydrothermal processes. Geochim. Cosmochim. Acta 171, 15–38.
Kuno, H., 1969. Pigeonite-bearing andesite and associated dacite from Asio, Japan. Am. J. Sci. Schairer 267, 257–268.
Li, D.-F., Chen, H.-Y., Hollings, P., Zhang, L.i., Sun, X.-M., Zheng, Y.i., Xia, X.-P., Xiao, B., Wang, C.-M., Fang, J., 2018. Trace element geochemistry of magnetite: Implications for ore genesis of the Talate skarn Pb-Zn (-Fe) deposit, Altay, NW China. Ore Geol. Rev. 100, 471–482.
Lindsley, D.H., 1981. Some experiments pertaining to the magnetite–ulvöspinel miscibility gap. Am. Mineral. 66, 759–762.
Liu, P.-P., Zhou, M.-F., Chen, W.T., Gao, J.-F., Huang, X.-W., 2015. In-situ LA-ICP-MS trace elemental analyses of magnetite: Fe–Ti–(V) oxide-bearing mafic–ultramafic layered intrusions of the Emeishan Large Igneous Province, SW China. Ore Geol. Rev. 65, 853–871.
Makvandi, S., Ghasemzadeh-Barvarz, M., Beaudoin, G., Grunsky, E.C., McClenaghan, M. B., Duchesne, C., Boutroy, E., 2016. Partial least squares-discriminant analysis of trace element compositions of magnetite from various VMS deposit subtypes: application to mineral exploration. Ore Geol. Rev. 78, 388–408.
Monteiro, L.V.S., Xavier, R.P., de Carvalho, E.R., Hitzman, M.W., Johnson, C.A., de Souza Filho, C.R., Torresi, I., 2008a. Spatial and temporal zoning of hydrothermal alteration and mineralization in the Sossego iron oxide–copper–gold deposit, Carajás Mineral Province, Brazil: paragenesis and stable isotope constraints. Miner. Deposita 43 (2), 129–159.
Monteiro, L.V.S., Xavier, R.P., Hitzman, M.W., Juliani, C., de Souza Filho, C.R., Carvalho, E.d.R., 2008b. Mineral chemistry of ore and hydrothermal alteration at the Sossego iron oxide–copper–gold deposit, Carajás Mineral Province, Brazil. Ore Geol. Rev. 34 (3), 317–336.
Moreto, C.P.N., Monteiro, L.V.S., Xavier, R.P., Creaser, R.A., DuFrane, S.A., Tassinari, C. C.G., Sato, K., Kemp, A.I.S., Amaral, W.S., 2015. Neoarchean and Paleoproterozoic iron oxide-copper-gold events at the Sossego Deposit, Carajás Province, Brazil: Re-Os and U-Pb geochronological evidence. Econ. Geol. 110, 809–835.
Nadoll, P., Mauk, J.L., Hayes, T.S., Koenig, A.E., Box, S.E., 2012. Geochemistry of magnetite from hydrothermal ore deposits and host rocks of the Mesoproterozoic Belt Supergroup, United States. Econ. Geol. 107 (6), 1275–1292.
Nadoll, P., Angerer, T., Mauk, J.L., French, D., Walshe, J., 2014. The chemistry of hydrothermal magnetite: a review. Ore Geol. Rev. 61, 1–32.
Neumann, E.-R., Svensen, H.H., Polozov, A.G., Hammer, Ø., 2017. Formation of Si-Al-Mg-Ca-rich zoned magnetite in an end-Permian phreatomagmatic pipe in the Tunguska Basin, East Siberia. Miner. Deposita 52 (8), 1205–1222.
Newberry, N.G., Peacor, D.R., Essene, E.J., Geissman, J.W., 1982. Silicon in magnetite: high resolution microanalysis of magnetite-ilmenite intergrowths. Contrib. Mineral. Petrol. 80 (4), 334–340.
Nielsen, R.L., Forsythe, L.M., Gallahan, W.E., Fisk, M.R., 1994. Major- and trace-element magnetite-melt equilibria. Chem. Geol. 117 (1-4), 167–191.
Ohkawa, M., Miyahara, M., Ohta, E., Hoshino, K., 2007. Silicon-substituted magnetite and accompanying iron oxides and hydroxides from the Kumano mine, Yamaguchi Prefecture, Japan: reexamination of the so-called maghemite (γ-Fe_2O_3). J. Mineral. Petrol. Sci. 102 (3), 182–193.
Ortoleva, P., Merino, E., Moore, C., Chadam, J., 1987. Geochemical self-organization I: reaction-transport feedbacks and modeling approach. Am. J. Sci. 287 (10), 979–1007.
Pisiak, L.K., Canil, D., Lacourse, T., Plouffe, A., Ferbey, T., 2017. Magnetite as an indicator mineral in the exploration of porphyry deposits: a case study in till near the Mount Polley Cu-Au deposit, British Columbia, Canada. Econ. Geol. 112 (4), 919–940.
Price, G.D., 1981a. Diffusion in the titanomagnetite solid solution series. Mineral. Mag. 44 (334), 195–200.
Price, G.D., 1981b. Subsolidus phase relations in the titanomagnetite solid solution series. Am. Mineral. 66, 751–758.
Putnis, A., Austrheim, H., 2013. Mechanisms of metasomatism and metamorphism on the local mineral scale: the role of dissolution-reprecipitation during mineral re-equilibration. In: Harlov, D.E., Austrheim, H. (Eds.), Metasomatism and the chemical transformation of rock: The role of fluids in terrestrial and extraterrestrial processes. Springer-Verlag, Berlin-Heidelberg, pp. 141–170.
Putnis, A., Fernandez-Diaz, L., Prieto, M., 1992. Experimentally produced oscillatory zoning in the (Ba, Sr)SO_4 solid solution. Nature 358 (6389), 743–745.
Reeder, R., Fagioli, R., Meyers, W., 1990. Oscillatory zoning of Mn in solution-grown calcite crystals. Earth Sci. Rev. 29 (1-4), 39–46.
Righter, K., Sutton, S.R., Newville, M., Le, L., Schwandt, C.S., Uchida, H., Lavina, B., Downs, R.T., 2006. An experimental study of the oxidation state of vanadium in spinel and basaltic melt with implications for the origin of planetary basalt. Am. Mineral. 91 (10), 1643–1656.
Shcheka, S.A., Romanenko, I.M., Chubarov, V.M., Kurentsova, N.A., 1977. Silica-bearing magnetites. Contrib. Mineral. Petrol. 63, 103–111.
Shimazaki, H., 1998. On the occurrence of silician magnetites. Resour. Geol. 48, 23–29.
Shore, M., Fowler, A.D., 1996. Oscillatory zoning in minerals: a common phenomenon. Can. Mineral. 34, 1111–1126.
Sievwright, R.H., Wilkinson, J.J., O'Neill, H.S.C., Berry, A.J., 2017. Thermodynamic controls on element partitioning between titanomagnetite and andesitic–dacitic silicate melts. Contrib. Mineral. Petrol. 172, 62.
Sievwright, R.H., O'Neill, H.S.C., Tolley, J., Wilkinson, J.J., Berry, A.J., 2020. Diffusion and partition coefficients of minor and trace elements in magnetite as a function of oxygen fugacity at 1150 °C. Contrib. Mineral. Petrol. 175, 40.
Sossi, P.A., Prytulak, J., O'Neill, H.S.C., 2018. Experimental calibration of vanadium partitioning and stable isotope fractionation between hydrous granitic melt and magnetite at 800°C and 0.5 GPa. Contrib. Mineral. Petrol. 173 (27).
Sun, X., Lin, H., Fu, Y., Li, D., Hollings, P., Yang, T., Liu, Z., 2017. Trace element geochemistry of magnetite from the giant Beiya gold-polymetallic deposit in Yunnan Province, Southwest China and its implications for the ore forming processes. Ore Geol. Rev. 91, 477–490.
Tan, W., Wang, C.Y., He, H.P., Liang, X.L., Liu, P., 2016. Mineralogy and origin of exsolution in Ti-rich magnetite from different magmatic Fe-Ti oxide-bearing intrusions. Can. Mineral. 54, 539–553.
Toplis, M.J., Corgne, A., 2002. An experimental study of element partitioning between magnetite, clinopyroxene and iron-bearing silicate liquids with particular emphasis on vanadium. Contrib. Mineral. Petrol. 144, 22–37.
Velasco, F., Tornos, F., Hanchar, J.M., 2016. Immiscible iron- and silica-rich melts and magnetite geochemistry at the El Laco volcano (northern Chile): evidence for a magmatic origin for the magnetite deposits. Ore Geol. Rev. 79, 346–366.
Verdugo-Ihl, M.R., Ciobanu, C.L., Cook, N.J., Ehrig, K.J., Courtney-Davies, L., 2020. Defining early stages of IOCG systems: evidence from iron oxides in the outer shell of the Olympic Dam deposit, South Australia. Miner. Deposita 55, 429–452.
Von Gruenewaldt, G., Klemm, D., Henckel, J., Dehm, R., 1985. Exsolution features in titanomagnetites from massive magnetite layers and their host rocks of the Upper Zone, Eastern Bushveld Complex. Econ. Geol. 80, 1049–1061.
Watson, E.B., 1996. Surface enrichment and trace-element uptake during crystal growth. Geochim. Cosmochim. Acta 60, 5013–5020.
Watson, E.B., Liang, Y., 1995. A simple model for sector zoning in slowly grown crystals: implications for growth rate and lattice diffusion, with emphasis on accessory minerals in crustal rocks. Am. Mineral. 80, 1179–1187.
Wen, G., Li, J.-W., Hofstra, A.H., Koenig, A.E., Lowers, H.A., Adams, D., 2017. Hydrothermal reequilibration of igneous magnetite in altered granitic plutons and its implications for magnetite classification schemes: insights from the Handan-Xingtai iron district, North China Craton. Geochim. Cosmochim. Acta 213, 255–270.
Westendorp, R.W., Watkinson, D.H., Jonasson, I.R., 1991. Silicon-bearing zoned magnetite crystals and the evolution of hydrothermal fluids at the Ansil Cu-Zn mine, Rouyn-Noranda, Quebec. Econ. Geol. 86, 1110–1114.

Xavier, R.P., Monteiro, L.V.S., Moreto, C.P.N., Pestilho, A.L.S., De Melo, G.H.C., Da Silva, M.A.D., Aires, B., Ribeiro, C., E Silva, F.H.F., 2012. The iron oxide copper-gold systems of the Carajás mineral province, Brazil. Econ. Geol. Special Publication 16, 433–454.

Xu, H., Shen, Z., Konishi, H., 2014. Si-magnetite nano-precipitates in silician magnetite from banded iron formation: Z-contrast imaging and ab initio study. Am. Mineral. 99, 2196–2202.

Yardley, B., Rochelle, C., Barnicoat, A., Lloyd, G., 1991. Oscillatory zoning in metamorphic minerals: an indicator of infiltration metasomatism. Mineral. Mag. 55, 357–365.

Yin, S., Ma, C., Robinson, P.T., 2017. Textures and high field strength elements in hydrothermal magnetite from a skarn system: implications for coupled dissolution-reprecipitation reactions. Am. Mineral. 102, 1045–1056.

Yin, S., Wirth, R., Ma, C., Xu, J., 2019. The role of mineral nanoparticles at a fluid-magnetite interface: implications for trace-element uptake in hydrothermal systems. Am. Mineral. 104, 1180–1188.